

# Reconstructing continuously heterogeneous structures from single particle cryo-EM with deep generative models

Ellen D. Zhong  
MIT  
zhong@mit.edu

Tristan Bepler  
MIT  
tbepler@mit.edu

Joseph H. Davis\*  
MIT  
jhdavis@mit.edu

Bonnie Berger\*  
MIT  
bab@mit.edu

## Abstract

Cryo-electron microscopy (cryo-EM) is a powerful technique for determining the structure of proteins and other macromolecular complexes at near-atomic resolution. In single particle cryo-EM, the central problem is to reconstruct the three-dimensional structure of a macromolecule from  $10^4$ – $10^7$  noisy and randomly oriented two-dimensional projections. However, the imaged protein complexes may exhibit structural variability, which complicates reconstruction and is typically addressed using discrete clustering approaches that fail to capture the full range of protein dynamics. Here, we introduce a novel method for cryo-EM reconstruction that extends naturally to modeling continuous generative factors of structural heterogeneity. This method encodes structures in Fourier space using coordinate-based deep neural networks, and trains these networks from unlabeled 2D cryo-EM images by combining exact inference over image orientation with variational inference for structural heterogeneity. We demonstrate that the proposed method, termed cryoDRGN, can perform *ab initio* reconstruction of 3D protein complexes from simulated and real 2D cryo-EM image data. To our knowledge, cryoDRGN is the first neural network-based approach for cryo-EM reconstruction and the first end-to-end method for directly reconstructing continuous ensembles of protein structures from cryo-EM images.

## 1 Introduction

In a single particle cryo-EM experiment, a purified solution of the target protein or biomolecular complex is frozen in a thin layer of vitreous ice and imaged at sub-nanometer resolution using an electron microscope. After initial preprocessing and segmentation of the raw data, the dataset typically comprises  $10^4$ – $10^7$  noisy projection images. Each image contains a separate instance of the molecule, recorded as the molecule’s electron density integrated along the imaging axis (Figure 1). A major bottleneck in cryo-EM structure determination is the computational task of 3D reconstruction, where the goal is to solve the inverse problem of learning the structure, i.e. the 3D electron density volume, which gave rise to the projection images. Unlike classic tomographic reconstruction (e.g. MRI), cryo-EM reconstruction is complicated by the unknown orientation of each copy of the molecule in the ice. Furthermore, cryo-EM reconstruction algorithms must handle challenges such as an extremely low signal to noise ratio (SNR), unknown in-plane translations, and imperfect signal transfer due to microscope optics. Despite these challenges, continuing advances in hardware [1, 2] and software [3, 4, 5] have enabled structure determination at near-atomic resolution for *rigid* proteins [6].

Many proteins and other biomolecules are intrinsically flexible and undergo large conformational changes to perform their function. Since each cryo-EM image contains a unique instance of the

---

\*Corresponding authors

molecule of interest, cryo-EM has the potential to resolve structural heterogeneity and uncover diverse functional states, which is experimentally infeasible with other structural biology techniques such as X-ray crystallography. However, this heterogeneity poses a substantial challenge for reconstruction as each image is no longer of the same structure. Traditional reconstruction algorithms address heterogeneity with discrete clustering approaches, however, protein conformations are continuous and may be poorly approximated with discrete clusters [7, 8].

Here, we introduce a neural network-based reconstruction algorithm that learns a continuous low-dimensional manifold over a protein’s conformational states from unlabeled 2D cryo-EM images. We present an end-to-end learning framework using an image encoder-volume decoder neural network architecture. Extending spatial-VAE [10], we formulate our decoder as a function of 3D Cartesian coordinates and unconstrained latent variables representing factors of image variation that we expect to result from protein structural heterogeneity. We perform all inference in Fourier space, which allows us to efficiently relate 2D projections to 3D volumes via the Fourier slice theorem [11]. By formulating our decoder as a function of Cartesian coordinates, we can explicitly model the imaging operation to disentangle the orientation of the molecule during imaging from intrinsic protein structural heterogeneity. Our learning framework avoids errant local minima in image orientation by optimizing with exact inference over a discretization of  $SO(3) \times \mathbb{R}^2$  using a branch and bound algorithm with frequency marching. The unconstrained latent variables are trained in the standard variational autoencoder [12] approach. We present results on both real and simulated cryo-EM data.

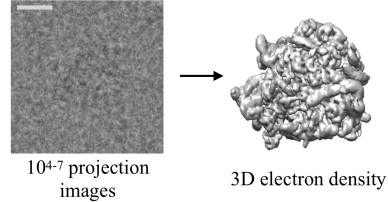


Figure 1: *Left*: Example cryo-EM image of a randomly oriented 80S ribosome embedded in ice [9]. *Right*: Reconstruction of the 80S ribosome’s 3D electron density, viewed at an isosurface. Scale bar denotes 100Å, and the length of the 80S ribosome is approximately 250Å.

## 2 Background and Notation

### 2.1 Image Formation Model

Cryo-EM aims to recover a structure of interest  $V : \mathbb{R}^3 \rightarrow \mathbb{R}$  consisting of an electron density at each point in space based on a collection of noisy images  $X_1, \dots, X_N$  produced by projecting (i.e. integrating) the volume in an unknown orientation along the imaging axis. Formally, the generation of image  $X$  can be modeled as:

$$X(r_x, r_y) = g * \int_{\mathbb{R}} V(R^T \mathbf{r} + t) dr_z + noise \quad \mathbf{r} = (r_x, r_y, r_z)^T \quad (1)$$

where  $V$  is the electron density (*volume*),  $R \in SO(3)$ , the 3D rotation group, is an unknown orientation of the volume, and  $t = (tx, ty, 0)$  is an unknown in-plane translation, corresponding to imperfect centering of the volume within the image. The image signal is convolved with  $g$ , the point spread function for the microscope – a different, but known<sup>2</sup>, frequency-dependent function for each image – before being corrupted with frequency-dependent noise and registered on a discrete grid of size  $D \times D$ , where  $D$  is the size of the image along one dimension.

The reconstruction problem is simplified by the observation that the Fourier transform of a 2D projection of  $V$  is a 2D slice through the origin of  $V$  in the Fourier domain, where the slice is perpendicular to the projection direction. This correspondence is known as the *Fourier slice theorem* [11]. In the Fourier domain, the generative process for image  $\hat{X}$  from volume  $\hat{V}$  can thus be written:

$$\hat{X}(k_x, k_y) = \hat{g}S(t)A(R)\hat{V}(k_x, k_y) + \epsilon \quad (2)$$

<sup>2</sup>The parameters of this function are estimated from the image data at a previous step of image processing and are typically treated as a known constant for the purposes of reconstruction

where  $\hat{g} = \mathcal{F}g$  is the contrast transfer function (CTF) of the microscope,  $S(t)$  is a phase shift operator corresponding to image translation by  $t$  in real space, and  $A(R)\hat{V} = \hat{V}(R^T(\cdot, \cdot, 0)^T)$  is a linear slice operator corresponding to rotation by  $R$  and linear projection along the z-axis in real space. The frequency-dependent noise  $\epsilon$  is typically modelled as independent, zero-centered Gaussian noise in Fourier space. Under this model, the probability of observing an image  $\hat{X}$  with pose  $\phi = (R, t)$  from volume  $\hat{V}$  is thus:

$$p(\hat{X}|\phi, \hat{V}) = p(\hat{X}|R, t, \hat{V}) = \frac{1}{Z} \exp \left( \sum_l \frac{-1}{2\sigma_l^2} \left| \hat{g}_l A_l(R)\hat{V} - S_l(t)\hat{X}_l \right|^2 \right) \quad (3)$$

where  $l$  is a two-component index over Fourier coefficients for the image,  $\sigma_l$  is the width of the Gaussian noise expected at each frequency, and  $Z$  is a normalization constant.

## 2.2 Traditional cryo-EM reconstruction

To recover the desired structure, cryo-EM reconstruction methods must jointly solve for the unknown volume  $V$  and image poses  $\phi_i = (R_i, t_i)$ . Expectation maximization and simpler variants of coordinate ascent [13] are typically employed to find a *maximum a posteriori* estimate of  $V$  marginalizing over the posterior distribution of  $\phi_i$ 's, i.e.:

$$V^{\text{MAP}} = \underset{V}{\operatorname{argmax}} \sum_{i=1}^N \log \int p(X_i|\phi, V)p(\phi)d\phi + \log p(V) \quad (4)$$

Intuitively, given  $V^{(n)}$ , the estimate of the volume at iteration  $n$ , images are first aligned with  $V^{(n)}$  (E-step), then with the updated alignments, the images are backprojected<sup>3</sup> to yield  $V^{(n+1)}$  (M-step). This iterative refinement procedure is sensitive to the initial estimate of  $V$  as the optimization objective is highly nonconvex; stochastic gradient descent is commonly used for *ab initio* reconstruction<sup>4</sup> to provide an initial estimate  $V^{(0)}$  [14].

Given sample heterogeneity, the standard approach in the cryo-EM field is to simultaneously reconstruct  $K$  independent volumes. Termed *multiclass refinement*, the image formation model is extended to assume images are generated from  $V_1, \dots, V_K$  independent volumes, with inference now requiring marginalization over  $\phi_i$ 's and class assignment probabilities  $\pi_j$ 's:

$$\underset{V_1, \dots, V_K}{\operatorname{argmax}} \sum_{i=1}^N \log \sum_{j=1}^K \left( \pi_j \int p(X_i|\phi, V_j)p(\phi)d\phi \right) + \sum_{j=1}^K \log p(V_j) \quad (5)$$

While this formulation is sufficiently descriptive when the structural heterogeneity consists of a small number of discrete conformations, it suffers when conformations cannot be summarized in a few discrete states or when conformations lie along a continuum of states. In practice, resolving such heterogeneity is handled through hierarchical multiclass refinement on subsets of the imaging dataset with manual choices for the number of classes and the initial models for refinement. Because the number and nature of the underlying structural states are unknown, this user-guided approach is error-prone and often leads to overfitting of some conformations, completely missing other sub-stoichiometric states, or producing blurring artifacts from continuous forms of heterogeneity. Furthermore, there exists an upper limit to the number of resolvable structures in this hierarchical approach as each class must have a minimum number of images to provide sufficient views for 3D reconstruction and to produce high resolution structures. In general, the identification and analysis of heterogeneity is an open problem in single particle cryo-EM.

## 3 Methods

We propose a neural network-based reconstruction method, cryoDRGN (Deep Reconstructing Generative Networks), that can perform *ab-initio* unsupervised reconstruction of a continuous distribution

<sup>3</sup>typically implemented as linear interpolation onto a 3D grid

<sup>4</sup>"Reconstruction" is used interchangeably in the cryo-EM literature to refer to either the full pipeline from *ab-initio* model generation followed by iterative refinement of the model via expectation maximization or solely to the latter. We focus on the former case.

over 3D volumes from unlabeled 2D images (Figure 2). We formulate an image encoder-volume decoder architecture based on the variational autoencoder (VAE) [12], where protein structural heterogeneity is modeled in the latent variable. While a standard VAE assumes all sources of image heterogeneity are entangled in the latent variable, we propose an architecture that enables modelling the intrinsic heterogeneity of the volume separately from the extrinsic orientation of the volume during imaging. Our end-to-end training framework explicitly models the forward image formation process to relate 2D views to 3D volumes and employs two separate strategies for inference: a variational approach for the unconstrained latent variables and a global search over  $SO(3) \times \mathbb{R}^2$  for the unknown pose of each image. These elements are described in further detail below.

### 3.1 Generative model

We design a deep generative model to approximate a single function,  $\hat{V} : \mathbb{R}^{3+n} \rightarrow \mathbb{R}$ , representing a  $n$ -dimensional manifold of 3D electron densities in the Fourier domain. Specifically, the volume  $\hat{V}$  is modelled as a probabilistic decoder  $p_\theta(\hat{V}|k, z)$ , where  $\theta$  are parameters of a multilayer perceptron (MLP). Given Cartesian coordinates  $k \in \mathbb{R}^3$  and continuous latent variable  $z$ , the decoder outputs distribution parameters for a Gaussian distribution over  $\hat{V}(k, z)$ , i.e. the electron density of volume  $\hat{V}_z$  at frequency  $k$  in Fourier space. Unlike a standard deconvolutional decoder which produces a separate distribution for each voxel of a  $D^3$  lattice given the latent variable, following spatial-VAE [10], we model a function over Cartesian coordinates. Here, these coordinates are explicitly treated as each pixel’s location in 3D Fourier space and thus enforce the topological constraints between 2D views in 3D via the Fourier slice theorem.

By the image formation model, each image corresponds to an *oriented* central slice of the 3D volume in the Fourier domain (Section 2). During training, the 3D coordinates of an image’s pixels can be explicitly represented by the rotation of a  $D \times D$  lattice initially on the x-y plane. Under this model, the log probability of an image,  $\hat{X}$ , represented as a vector of size  $D \times D$ , given the current MLP, latent pose variables  $R \in SO(3)$  and  $t \in \mathbb{R}^2$ , and unconstrained latent variable,  $z$ , is:

$$\log p(\hat{X}|R, t, z) = \log p(\hat{X}'|R, z) = \sum_i \log p_\theta(\hat{V}|R^T c_0^{(i)}, z) \quad (6)$$

where  $i$  indexes over the coordinates of a fixed lattice  $c_0$ . Note that  $\hat{X}' = S(-t)\hat{X}$  is the centered image, where  $S$  is the phase shift operator corresponding to image translation in real space. We define  $c_0$  as a vector of 3D coordinates of a fixed lattice spanning  $[-0.5, 0.5]^2$  on the x-y plane to represent the unoriented coordinates of an image’s pixels.

Instead of directly supplying  $k$ , a fixed positional encoding of  $k$  is supplied to the decoder, consisting of sine and cosine waves of varying frequency:

$$pe^{(2i)}(k_j) = \sin(k_j D \pi (2/D)^{2i/D}), \quad i = 1, \dots, D/2; k_j \in k \quad (7)$$

$$pe^{(2i+1)}(k_j) = \cos(k_j D \pi (2/D)^{2i/D}), \quad i = 1, \dots, D/2; k_j \in k \quad (8)$$

Without loss of generality, we assume a length scale by our definition of  $c_0$  which restricts the support of the volume to a sphere of radius 0.5. The wavelengths of the positional encoding thus follow a geometric series spanning the Fourier basis from wavelength 1 to the Nyquist limit ( $2/D$ ) of the image data. While this encoding empirically works well for noiseless data, we obtain better results with a slightly modified featurization for noisy datasets consisting of a geometric series which excludes the top 10 percentile of highest frequency components of the noiseless positional encoding.

### 3.2 Inference

We employ a standard VAE for approximate inference of the latent variable  $z$ , but use a global search to infer the pose  $\phi = (R, t)$  using a branch and bound algorithm.

As each cryo-EM image is a noisy projection of an instance of the volume at a random, unknown pose (viewing direction), the image encoder aims to learn a *pose-invariant* representation of the protein’s structural heterogeneity. Following the standard VAE framework, the probabilistic encoder  $q_\xi(z|\hat{X})$



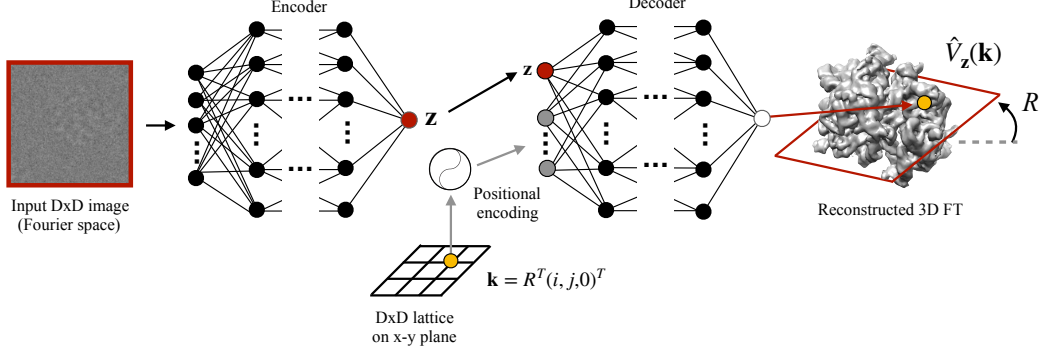


Figure 2: CryoDRGN model architecture. We use a VAE to perform approximate inference for latent variable  $z$  denoting image heterogeneity. The decoder reconstructs an image pixel by pixel given  $z$  and  $pe(k)$ , the positional encoding of 3D Cartesian coordinates. The 3D coordinates corresponding to each image pixel are obtained by rotating a DxD lattice on the x-y plane by  $R$ , the image orientation. The latent orientation for each image is inferred through a branch and bound global optimization procedure (not shown).

is a MLP with variational parameters  $\xi$  and Gaussian output with diagonal covariance. Given an input cryo-EM image  $\hat{X}$ , represented as a DxD vector, the encoder MLP outputs  $\mu_{z|\hat{X}}$  and  $\Sigma_{z|\hat{X}}$ , statistics that parameterize an approximate posterior to the intractable true posterior  $p(z|\hat{X})$ . The prior on  $z$  is a standard normal,  $\mathcal{N}(0, \mathbf{I})$ .

Predicting the pose for each image directly with the variational encoder performs poorly as the loss has spurious local minima in  $\phi$ . Inspired by traditional reconstruction algorithms [14], we instead perform a global search over  $SO(3) \times \mathbb{R}^2$  for the maximum-likelihood pose for each image given the current decoder MLP and a sampled value of  $z$  from the approximate posterior. Two techniques are used to improve the efficiency of the search over poses: (1) discretizing the search space on a uniform grid and sub-dividing grid points after pruning candidate poses with *branch and bound* (BNB), and (2) band pass limiting the objective to low frequency components and incrementally increasing the k-space limit at each iteration (*frequency marching*). The pose inference procedure encodes the intuition that low-frequency components dominate pose estimation, and is fully described in Appendix A.

In summary, for a given image  $\hat{X}_i$ , the image encoder produces  $\mu_{z|\hat{X}_i}$  and  $\Sigma_{z|\hat{X}_i}$ . A sampled value of the latent  $z_i \sim \mathcal{N}(\mu_{z|\hat{X}_i}, \Sigma_{z|\hat{X}_i})$  is broadcast to all pixels. Given  $z_i$  and the current decoder, BNB orientational search identifies the maximum likelihood rotation  $R_i$  and translation  $t_i$  for  $\hat{X}_i$ . The decoder  $p_\theta$  then reconstructs the image pixel by pixel given the positional encoding of  $R_i^T c_0$  and  $z_i$ . The phase shift corresponding to  $t_i$  and optionally the CTF  $\hat{g}_i$  is then applied on the reconstructed pixel intensities. In certain experiments, we treat the CTF by phase-flipping the input images instead.

Following the standard VAE framework, the optimization objective is the variational lower bound of the model evidence:

$$\mathcal{L}(\hat{X}_i; \xi, \theta) = \mathbb{E}_{q_\xi(z|\hat{X}_i)}[\log p_\theta(\hat{X}_i|z)] - KL(q_\xi(z|\hat{X}_i)||p(z)) \quad (9)$$

where the first term encourages  $p_\theta$  to reconstruct input image  $\hat{X}$  and the second term encourages the approximate posterior to be close to the prior. Stochastic gradient descent is used to update network weights  $\theta$  and  $\xi$ .

By comparing many 2D slices from the imaging dataset, the volume can be learned through feedback from these single views. Furthermore, this learning process is denoising as overfitting to noise from a single image would lead to higher reconstruction error for other views.

At test time, volumes along the learned latent manifold may be estimated from  $p_\theta$  via *maximum a posteriori* (MAP) estimation given a value of  $z$  and a 3D lattice spanning  $[-0.5, 0.5]^3$ . Additionally, we can use  $q_\xi$  to generate the latent encoding for each image, defined as  $\arg\max_z q_\xi(z|\hat{X}_i)$ , and view the distribution of images on the learned latent manifold.

We note that the distribution of 3D volumes models heterogeneity within a single imaging dataset, capturing structural variation for a particular protein or biomolecular complex, and that a separate network is trained per experimental dataset.

### 3.3 Implementation and training details

Given an imaging dataset,  $\hat{X}_1, \dots, \hat{X}_N$ , we summarize three training paradigms of cryoDRGN. 1) For homogeneous reconstruction, we only train the volume decoder  $p_\theta$  and perform BNB pose inference for the unknown  $\phi_i$ 's for each image. 2) As an intermediate task, we can perform heterogeneous reconstruction training the image encoder  $q_\xi$  and the volume decoder  $p_\theta$  with known  $\phi_i$ 's to skip BNB pose inference. 3) For fully unsupervised heterogeneous reconstruction, we jointly train  $q_\xi$  and  $p_\theta$  to learn a continuous latent representation, performing BNB pose inference for the unknown pose of each image.

Unless otherwise specified, the encoder and decoder networks are both MLPs containing 10 hidden layers of dimension 128 with ReLU activations. A fully connected architecture is used instead of a convolutional architecture because the images are not represented in real space.

Instead of representing both the real and imaginary components of each image, we use the closely-related Hartley space representation [15]. The Hartley transform of real-valued functions is equivalent to the real minus imaginary component of the FT, and thus is real valued. The Fourier slice theorem still holds and the error model is equivalent.

In this work, we simplify the image generation model to Gaussian white noise. Therefore, for a given image, the negative log likelihood for a reconstructed slice from the decoder corresponds to the mean squared error between the phase-shifted image and the oriented slice from the volume decoder. We leave the implementation of a colored noise model to future work.

We use the Adam optimizer [16] with learning rate of  $5e-4$  for experiments involving noiseless, homogeneous datasets, and  $1e-4$  for all other experiments. All models are implemented in Pytorch [17] with user-friendly software in preparation.

## 4 Related Work

**Homogeneous cryo-EM reconstruction:** Cryo-EM reconstruction is typically accomplished in two stages: 1) generation of an initial low-resolution model followed by 2) iterative refinement of the initial model with a coordinate ascent procedure alternating between projection matching and refinement of the structure. In practice, initial structures can be obtained experimentally [18], inferred based on homology to complexes with known structure, or via *ab-initio* reconstruction with stochastic gradient descent [14]. There also exist a diversity of theoretical approaches for *ab initio* reconstruction based on the common lines principle [19, 20, 21]. Once an initial model is generated, there are many tools for iterative refinement of the model [4, 14, 22, 23, 24]. For example, [13] presents a Bayesian approach based on a probabilistic model of the image formation process and refines the structure via Expectation Maximization. Frequency marching is used extensively in existing tools to speed up the search for the optimal pose for each image [4, 25, 23, 14]. State-of-the-art cryoSPARC [14] implements a branch and bound optimization scheme, where their bound is a probabilistic lower bound based on the noise characteristics from the image formation model.

**Heterogeneous cryo-EM reconstruction:** In the cryo-EM literature, standard approaches for addressing structural heterogeneity use mixture models of discrete, independent volumes in either 2D [26] or 3D (e.g. multiclass refinement) [27, 23]. These mixture models assume that the clusters are independent and homogeneous, and in practice require many rounds of expert-guided hierarchical clustering from appropriate initial volumes and manual choices for number of clusters.

More recently, [8] proposed multibody refinement, an iterative refinement method for heterogeneous reconstruction that imposes structural assumptions on the protein. Based on a user-drawn mask from an initial homogeneous reconstruction, the image generative model is extended to model the protein as a sum of rigid bodies that move independently in a pairwise fashion, allowing for independent motion up to  $\pm 30^\circ$  from the consensus reconstruction.

Theoretical work using techniques from statistical manifold embedding aim to build a continuous manifold of the images [28], and have been applied to analyze existing datasets [29]. However, this

method assumes that image heterogeneity cannot be dominated by imaging orientation and requires an initial clustering of images by viewing direction. Furthermore, the final structures are obtained by clustering the images along the manifold and reconstructing with traditional tools.

Recent theoretical work for continuous heterogeneous reconstruction includes expansion of discrete 3D volumes in a basis of Laplacian eigenvectors [30] and a general framework for modelling hyper-volumes [31] e.g. as a tensor product of spatial and temporal basis functions [32]. To our knowledge, our work is the first to apply deep neural networks to cryo-EM reconstruction, and in doing so, is the first that can learn a continually heterogeneous volume from real cryo-EM data.

**Neural network 3D reconstruction in computer vision:** There is a large body of work in computer vision on 3D object reconstruction from 2D viewpoints. While these general approaches have elements in common with single particle cryo-EM reconstruction, the problem in the context of computer vision differs substantially in that 2D viewpoints are not projections and viewing directions are known [33, 34, 35, 36]. For example, [34] propose a neural network that can predict a 3D volume from a single 2D viewpoint using only 2D image supervision. [35] learn a generative model over 3D object shapes based on 2D images of the objects thereby disentangling variation in shape and pose. [36] also reconstruct and disentangle the shape and pose of 3D objects from 2D images by enforcing geometric consistency. These works attempt to encode the viewpoint ‘projection’ operation<sup>5</sup> explicitly in the model in a manner similar to our use of the Fourier slice theorem.

**Coordinate-based neural networks in computer vision:** Using spatial (i.e. pixel) coordinates as features to a convolutional decoder to improve generative modeling has been proposed many times, with recent work computing each image as a function of a fixed coordinate lattice and latent variables [37]. However, directly modeling a function that maps spatial coordinates to values is less extensively explored. In CocoNet [38], the authors present a deep neural network that maps 2D pixel coordinates to RGB color values. CocoNet learns an image model for single images, using the capacity of the network to memorize the image, which can then be used for various tasks such as denoising and upsampling. Similarly, Spatial-VAE [10] proposes a similar coordinate-based image model to enforce geometric consistency between rotated 2D images in order to learn latent image factors and disentangle positional information from image content. Our method extends many of these ideas from simpler 2D image modelling to enable 3D cryo-EM reconstruction in the Fourier domain.

## 5 Results

Here, we present both qualitative and quantitative results for 1) homogeneous cryo-EM reconstruction, validating that our cryoDRGN reconstructed volumes match those from existing tools; 2) heterogeneous cryo-EM reconstruction first with pose supervision, demonstrating automatic learning of the latent manifold that previously required many expert-guided rounds of multiclass refinement; and 3) fully unsupervised heterogeneous reconstruction, demonstrating cryoDRGN’s ability to reconstruct a continuous manifold of heterogeneous protein structures, a capability not provided by any existing tool.

### 5.1 CryoDRGN can perform unsupervised homogeneous reconstruction

We first evaluate cryoDRGN on homogeneous datasets, where existing tools are capable of reconstruction, and validate that cryoDRGN inferred poses and reconstructed volumes match those from state-of-the-art tools.

*Datasets:* To evaluate cryoDRGN for homogeneous reconstruction, we test on two synthetic and one real dataset. To create the synthetic homogeneous datasets, we simulate 50k projections (image size  $D=128$ ) of the large ribosomal subunit following the cryo-EM image formation model by 1) rotating the 3D volume in real space by  $R$ , where  $R \in SO(3)$  is sampled uniformly, 2) projecting the volume along the z-axis, 3) shifting the resulting 2D image by  $t$ , where  $t$  is sampled uniformly from  $[-10, 10]^2$  pixels, and 4) optionally adding noise to a signal to noise ratio (SNR) of 0.1, a typical value for cryo-EM [39]. For the real dataset, we use the images from EMPIAR-10028 [9] consisting of 105,247 images of the 80S ribosome assumed to be homogeneous and downsampled to image size  $D=90$  (further details in Appendix B).

<sup>5</sup>This is not the meaning of projection in the context of this work, where it refers to *integration* along the imaging axis.

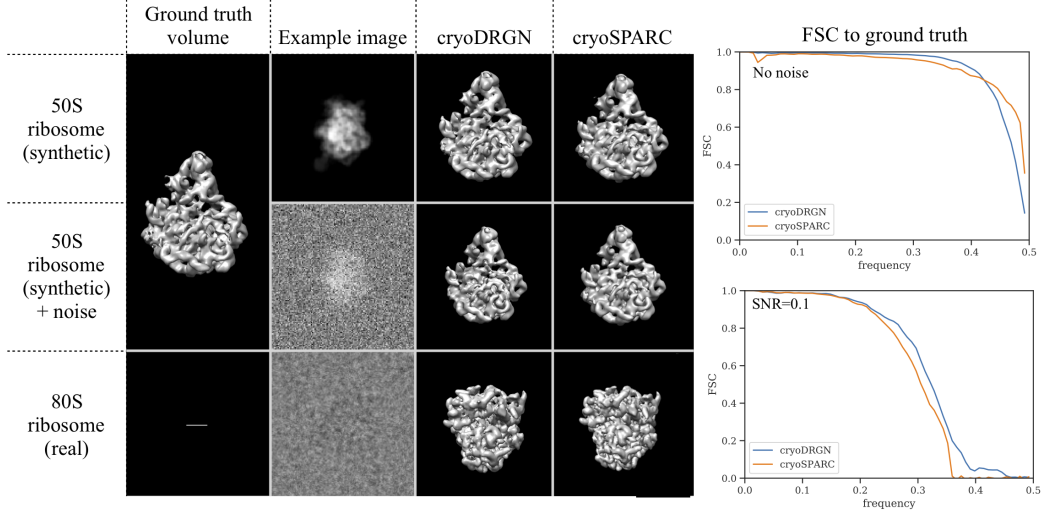


Figure 3: CryoDRGN unsupervised homogeneous reconstruction matches state-of-the-art. (left) Reconstructed volumes from cryoDRGN and cryoSPARC on 2 simulated datasets and 1 real cryoEM dataset. (right) Fourier shell correlation (FSC) curves between the reconstructed volume and the ground truth volume for the synthetic ribosome datasets.

*Training and runtime:* For each dataset, we train the volume decoder (10 hidden layers of dimension 128) in minibatches of 10 images with random orientations for the first epoch to learn a volume with roughly correct spatial extent, followed by 4 epochs with branch and bound (BNB) pose inference (30 min/epoch noiseless, 80 min/noisy datasets). Since BNB pose inference is the bottleneck during training, we employ a multiscale training protocol, where after 4 epochs with BNB pose inference, the latent pose is fixed, and we train a separate, larger volume decoder (10 hidden layers of dimension 500) for 15 epochs with fixed poses to "refine" the structure to high resolution (20 min/epoch). Training times are reported for 50k, D=128 image datasets trained on a Nvidia Titan V GPU. We leave the evaluation of cryoDRGN on larger image sizes that contain higher resolution information and the determination of heuristics for network size and training regimes to future work.

As a baseline for comparison, we perform homogeneous *ab-initio* reconstruction followed by iterative refinement in cryoSPARC [14]. We compare against cryoSPARC as a representative of traditional state-of-the-art tools, which all implement variants of the same algorithm (Section 2).

*Results:* CryoDRGN can perform unsupervised *ab-initio* homogeneous reconstruction of 3D volumes comparably to state-of-the-art tools. In Figure 3 (left), we show cryoDRGN and cryoSPARC reconstructed volumes along with the ground truth volume if it exists. The similarity of the structures can be quantified with the Fourier shell correlation (FSC) curve<sup>6</sup> between the reconstructed volumes and the ground truth structure (Figure 3 right). Pose errors are given in Table 1 showing comparable performance between cryoDRGN and cryoSPARC. For the real cryoEM dataset (no ground truth), the median pose difference between cryoDRGN and cryoSPARC reconstructions is 0.002 for rotations and 1.0 pixels for translations, and the resulting volumes are correlated as measured by a FSC = 0.5 up to the Nyquist resolution limit for this dataset (10.72 Å).

Method	Dataset	
	No Noise	SNR=0.1
cryoSPARC	0.0009 \ 0.47	0.002 \ 0.64
cryoDRGN	0.0004 \ 0.27	0.003 \ 0.38

Table 1: Homogeneous reconstruction pose accuracy quantified by median rotation/translation error. Rotation error is defined as the Frobenius norm of the predicted 3D rotation matrix and the rotation matrix from the ground truth projections, computed after alignment. Translation error is defined as the L2 norm between predicted and ground truth translation.

<sup>6</sup>The FSC curve measures correlation between volumes as a function of radial shells in Fourier space. The field currently lacks a rigorous method for measuring the quality of reconstruction. In practice, however, resolution is often reported as  $1/k_0$  where  $k_0 = \text{argmax}_k FSC(k) < C$  and  $C$  is some fixed threshold.

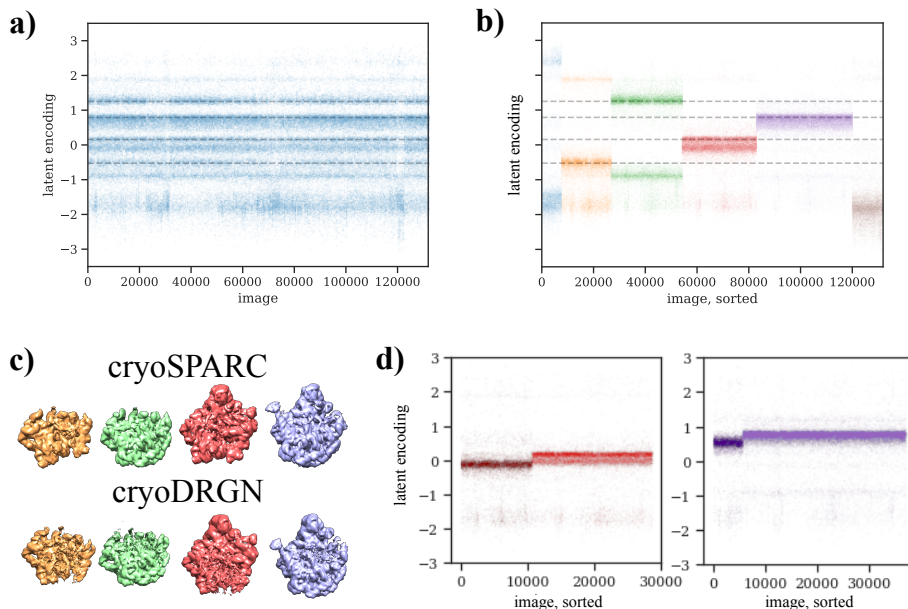


Figure 4: CryoDRGN heterogeneous reconstruction identifies major structural states for large ribosomal subunit assembly. *a)* CryoDRGN latent encoding for each image of EMPIAR-10076 implies a mixture of discrete states. *b)* The latent encoding aligns with image cluster assignment from a 6 class discrete multiclass refinement performed in cryoSPARC using the published structures as initial models for refinement. Images are sorted and their latent encoding is colored according to cryoSPARC cluster assignment. *c)* Volumes sampled along the latent space (at dashed lines in *b)*) qualitatively match the cryoSPARC volumes for the large ribosomal subunit. *d)* The latent encoding aligns with cluster assignments from a successive round of multiclass refinement in cryoSPARC on the subset of images from the purple and red classes in *b)*. Images are sorted and their latent encoding is shaded according to their cluster assignment.

## 5.2 CryoDRGN automatically learns discrete heterogeneity in real cryo-EM data

Next, we evaluate cryoDRGN for heterogeneous cryo-EM reconstruction on a real dataset and demonstrate automatic learning of the latent manifold that previously required many expert-guided rounds of clustering. Here, poses are obtained through alignment to an existing structure and treated as known, which speeds up training by roughly 2 orders of magnitude.

*Dataset:* We consider the dataset from EMPIAR-10076 [40] which contains 131,899 images of the *E. coli* large ribosomal subunit in various stages of assembly. Images were downsampled to  $D=128$  (Nyquist limit of  $6.55\text{\AA}$ ). Poses were determined by aligning the images to a mature large ribosomal subunit structure and are then treated as a known constant during training. In the original analysis of this dataset [40], multiple rounds of multiclass refinement with varying number of classes followed by human comparison of similar volumes were used to identify 4 major structural states of the large ribosomal subunit and 2 additional structures from impurities during sample preparation.

*Training and runtime:* We train cryoDRGN with a 1-D latent variable in minibatches of 10 images for 200 epochs, treating image pose as fixed (11 min/epoch on a Nvidia Titan V GPU for this dataset). To test that the learned encoding captures the known structural states, we perform multiclass refinement in cryoSPARC (a discrete mixture model of volumes) as a proxy for the published multiclass refinement results since the image assignment to classes was not published. We use the 6 published structures from [40] low pass filtered as initial models for cryoSPARC multiclass refinement and confirm the correspondence between the reconstructed structures in cryoSPARC with the published volumes (Figure S1). Further baseline and training details are given in Appendix C.

*Results:* CryoDRGN automatically identifies all 4 major states that were originally identified through manual comparison of volumes [40]. Figure 4a shows the latent encoding for each image in the dataset ( $\arg\max_z q_\xi(z|\hat{X})$ ), which implies a discrete clustering of states. In Figure 4b, we sort images and color their latent encoding according to MAP cluster assignment from cryoSPARC, and

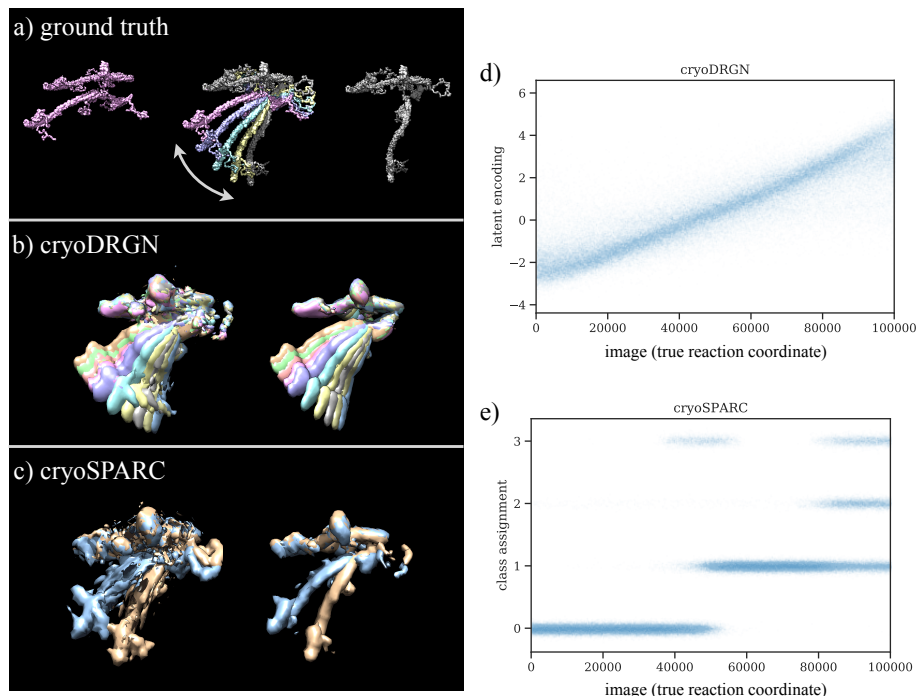


Figure 5: CryoDRGN can perform unsupervised heterogeneous reconstruction of a dataset containing continuous variability. a) Ground truth atomic model of a protein complex containing one degree of freedom, transforming from the left (pink) to the right (grey) structure. b) CryoDRGN fully unsupervised heterogeneous reconstruction with a 1-D latent variable reconstructs the full 1-D manifold of structures. We show 10 structures sampled along the latent space, viewed at high and low isosurface. c) Discrete multiclass reconstruction in cryoSPARC with 4 classes yielded 2 highly populated classes (blue and orange), viewed at high and low isosurface. d) The cryoDRGN latent encoding for each image, where images are ordered along the ground truth reaction coordinate. e) Class assignment for each image from cryoSPARC.

find that the learned latent manifold aligns with cryoSPARC clusters. Volumes sampled along the latent space correspond to the structures of the 4 major classes of the large ribosomal subunit (Figure 4c). Quantitative comparison with FSC curves and additional structures are shown in Figure S2. Multiple values of the latent are captured in some of the cryoSPARC clusters, and a successive round of multiclass refinement on the subset of images from the red and purple classes in cryoSPARC aligns with the latent subclusters (Figure 4d).

We note that 2 of 6 published structures correspond to impurities in the sample, and while the latent encoding clustered the images corresponding to these impurities separately from images corresponding to the large ribosomal subunit (blue and brown in Figure 4b), the sampled volumes for these states are uninterpretable as image poses were determined by aligning to the large ribosomal subunit structure. A deeper analysis of the correspondence between the learned latent manifold and the biological states of large ribosomal subunit assembly, while beyond the scope of this work, poses an interesting question for future applications.

### 5.3 CryoDRGN can perform fully unsupervised heterogeneous reconstruction

We perform fully unsupervised heterogeneous reconstruction with cryoDRGN and demonstrate cryoDRGN’s ability to reconstruct a continuous manifold of structures from a heterogeneous dataset.

**Dataset:** We generate a dataset containing one continuous degree of freedom as follows: From an atomic model of a protein complex (Figure 5a), we rotate a single bond in the atomic model while keeping the remaining structure fixed, and sample 200 atomic models along this reaction coordinate. 500 projections with random rotations and in-plane translations are generated for each model ( $D=64$ ), yielding a total of 100k images, approximating a uniform distribution along a continuous reaction coordinate. The box size of the model is  $720\text{\AA}$  and the Nyquist limit is  $22.5\text{\AA}$  for this dataset.



*Training and runtime:* We train cryoDRGN with a 1-D latent variable in minibatches of 5 images with random angles for the first epoch and BNB pose inference for 4 epochs. We then fix poses from the final iteration of BNB and continue training the encoder and decoder networks for 10 more epochs (120 min/epoch vs 2 min/epoch with and without BNB pose inference, respectively, on a Nvidia Titan V GPU). As a baseline, we perform multiclass reconstruction in cryoSPARC with K=4 classes (>4 fails) starting with *ab-initio* heterogeneous reconstruction to generate initial models followed by discrete multiclass refinement.

*Results:* CryoDRGN is able to learn the entire manifold of structures (Figure 5b), whereas discrete multiclass reconstruction with cryoSPARC (Figure 5c) produces 2 originally unaligned structures with blurring artifacts. Note that while we only show volumes at 10 samples of the latent variable in Figure 5b, the volume decoder is able to generate a continuum of structures.

We can quantitatively measure performance on this task with an FSC resolution metric between the *maximum a posteriori*  $V_{z_i|\hat{X}_i}$  either estimated from  $q_\xi$  and  $p_\theta$  or from the discrete class assignment in cryoSPARC and the ground truth volume which generated each image, averaged across images in the dataset and find **2.00** vs 3.21 pixel resolution (FSC=0.143 criterion) and **2.06** vs 8.76 pixel resolution (FSC=0.5 criterion) for **cryoDRGN** vs. cryoSPARC (lower is better; best possible is 2 pixels).

In Figure 5d, we show the latent encoding for each image in the dataset ( $\arg\max_z q_\xi(z|\hat{X})$ ), where images are ordered along the ground truth reaction coordinate. The latent encoding varies smoothly with the ground truth reaction coordinate whereas in Figure 5e, cryoSPARC clusters the majority of images between two, assumed-homogeneous classes.

## 6 Conclusions

We present a novel neural network-based reconstruction method for single particle cryo-EM that learns continuous variation in protein structure. We applied cryoDRGN on a real dataset of highly heterogeneous ribosome assembly intermediates and demonstrate automatic partitioning of structural states, where previous methods required many rounds of expert-guided hierarchical clustering. In the presence of simulated continuous heterogeneity, we show that cryoDRGN learns a continuous representation of structure along the true reaction coordinate, effectively disentangling imaging orientation from intrinsic structural heterogeneity. This work provides a new method for cryo-EM practitioners to analyze structural variability, which can aid in understanding the relationship between protein structure and function. The techniques described here may also have broader applicability to image and volume generative modelling in other domains of computer vision.

## 7 Acknowledgements

We thank Ben Demeo, Ashwin Narayan, Adam Lerer, and Kotaro Kelley for helpful discussions and feedback. This work was funded by the National Science Foundation Graduate Research Fellowship Program, NIH grant R01-GM081871, NIH grant R00-AG050749, and the MIT J-Clinic for Machine Learning and Health.

## References

- [1] Werner Kühlbrandt. Cryo-EM enters a new era. *eLife*, 3:e03678, August 2014.
- [2] Kühlbrandt, Werner. Biochemistry. The resolution revolution. *Science*, 343(6178):1443–1444, March 2014.
- [3] Xueming Li, Paul Mooney, Shawn Zheng, Christopher R Booth, Michael B Braunfeld, Sander Gubbens, David A Agard, and Yifan Cheng. Electron counting and beam-induced motion correction enable near-atomic-resolution single-particle cryo-EM. *Nature methods*, 10(6):584–590, June 2013.
- [4] Sjors H W Scheres. RELION: implementation of a Bayesian approach to cryo-EM structure determination. *Journal of structural biology*, 180(3):519–530, December 2012.
- [5] Sjors H W Scheres and Shaoxia Chen. Prevention of overfitting in cryo-EM structure determination. *Nature methods*, 9(9):853–854, September 2012.

- [6] Jean-Paul Renaud, Ashwin Chari, Claudio Ciferri, Wen-Ti Liu, Hervé-William Rémigy, Holger Stark, and Christian Wiesmann. Cryo-EM in drug discovery: achievements, limitations and prospects. *Nature reviews. Drug discovery*, 17(7):471–492, July 2018.
- [7] Pooja Malhotra and Jayant B Udgaonkar. How cooperative are protein folding and unfolding transitions? *Protein science : a publication of the Protein Society*, 25(11):1924–1941, November 2016.
- [8] Takanori Nakane, Dari Kimanius, Erik Lindahl, and Sjors Hw Scheres. Characterisation of molecular motions in cryo-EM single-particle data by multi-body refinement in RELION. *eLife*, 7:e36861, June 2018.
- [9] Wong, Wilson, Bai, Xiao-Chen, Brown, Alan, Fernandez, Israel S, Hanssen, Eric, Condron, Melanie, Tan, Yan Hong, Baum, Jake, and Scheres, Sjors H W. Cryo-EM structure of the Plasmodium falciparum 80S ribosome bound to the anti-protozoan drug emetine. *eLife*, 3:e01963, June 2014.
- [10] Tristan Bepler, Ellen Zhong, Kotaro Kelley, Edward Brignole, and Bonnie Berger. Explicitly disentangling image content from rotation and translation with spatial-VAE. *Neural Information Processing Systems (NeurIPS)*, 2019.
- [11] Ronald N Bracewell. Strip integration in radio astronomy. *Australian Journal of Physics*, 9(2):198–217, 1956.
- [12] Diederik P Kingma and Max Welling. Auto-encoding variational bayes. In *The 2nd International Conference on Learning Representations (ICLR)*, 2013.
- [13] Sjors H W Scheres. A Bayesian view on cryo-EM structure determination. *Journal of molecular biology*, 415(2):406–418, January 2012.
- [14] Ali Punjani, John L Rubinstein, David J Fleet, and Marcus A Brubaker. cryoSPARC: algorithms for rapid unsupervised cryo-EM structure determination. *Nature methods*, 14(3):290–296, March 2017.
- [15] Ralph VL Hartley. A more symmetrical fourier analysis applied to transmission problems. *Proceedings of the IRE*, 30(3):144–150, 1942.
- [16] Diederik P Kingma and Jimmy Ba. Adam: A method for stochastic optimization. *arXiv preprint arXiv:1412.6980*, 2014.
- [17] Adam Paszke, Sam Gross, Soumith Chintala, Gregory Chanan, Edward Yang, Zachary DeVito, Zeming Lin, Alban Desmaison, Luca Antiga, and Adam Lerer. Automatic differentiation in pytorch. 2017.
- [18] Andres E Leschziner and Eva Nogales. The orthogonal tilt reconstruction method: an approach to generating single-class volumes with no missing cone for ab initio reconstruction of asymmetric particles. *Journal of structural biology*, 153(3):284–299, 2006.
- [19] Ido Greenberg and Yoel Shkolnisky. Common lines modeling for reference free Ab-initio reconstruction in cryo-EM. *Journal of structural biology*, 200(2):106–117, November 2017.
- [20] Dominika Elmlund and Hans Elmlund. SIMPLE: Software for ab initio reconstruction of heterogeneous single-particles. *Journal of structural biology*, 180(3):420–427, December 2012.
- [21] Lanhui Wang, Amit Singer, and Zaiwen Wen. Orientation Determination of Cryo-EM Images Using Least Squared Deviations. *SIAM journal on imaging sciences*, 6(4):2450–2483, December 2013.
- [22] Michael Hohn, Grant Tang, Grant Goodyear, P R Baldwin, Zhong Huang, Pawel A Penczek, Chao Yang, Robert M Glaeser, Paul D Adams, and Steven J Ludtke. SPARX, a new environment for Cryo-EM image processing. *Journal of structural biology*, 157(1):47–55, January 2007.
- [23] Lyumkis, Dmitry, Brilot, Axel F, Theobald, Douglas L, and Grigorieff, Nikolaus. Likelihood-based classification of cryo-EM images using FREALIGN. *Journal of structural biology*, 183(3):377–388, September 2013.
- [24] Guang Tang, Liwei Peng, Philip R Baldwin, Deepinder S Mann, Wen Jiang, Ian Rees, and Steven J Ludtke. EMAN2: an extensible image processing suite for electron microscopy. *Journal of structural biology*, 157(1):38–46, January 2007.
- [25] Alex Barnett, Leslie Greengard, Andras Pataki, and Marina Spivak. Rapid solution of the cryo-EM reconstruction problem by frequency marching. *arXiv.org*, October 2016.



- [26] Sjors HW Scheres, Mikel Valle, Rafael Nuñez, Carlos OS Sorzano, Roberto Marabini, Gabor T Herman, and Jose-Maria Carazo. Maximum-likelihood multi-reference refinement for electron microscopy images. *Journal of molecular biology*, 348(1):139–149, 2005.
- [27] Sjors HW Scheres. Maximum-likelihood methods in cryo-em. part ii: Application to experimental data. *Methods in enzymology*, 482:295, 2010.
- [28] Joachim Frank and Abbas Ourmazd. Continuous changes in structure mapped by manifold embedding of single-particle data in cryo-EM. *Methods (San Diego, Calif.)*, 100:61–67, May 2016.
- [29] Ali Dashti, Peter Schwander, Robert Langlois, Russell Fung, Wen Li, Ahmad Hosseinizadeh, Hstau Y Liao, Jesper Pallesen, Gyanesh Sharma, Vera A Stupina, Anne E Simon, Jonathan D Dinman, Joachim Frank, and Abbas Ourmazd. Trajectories of the ribosome as a Brownian nanomachine. *Proceedings of the National Academy of Sciences of the United States of America*, 111(49):17492–17497, December 2014.
- [30] Amit Moscovich, Amit Halevi, Joakim Andén, and Amit Singer. Cryo-EM reconstruction of continuous heterogeneity by Laplacian spectral volumes. *arXiv.org*, July 2019.
- [31] Roy R Lederman, Joakim Andén, and Amit Singer. Hyper-Molecules: on the Representation and Recovery of Dynamical Structures, with Application to Flexible Macro-Molecular Structures in Cryo-EM. *arXiv.org*, July 2019.
- [32] Roy R Lederman and Amit Singer. Continuously heterogeneous hyper-objects in cryo-EM and 3-D movies of many temporal dimensions. *arXiv.org*, April 2017.
- [33] Vincent Sitzmann, Justus Thies, Felix Heide, Matthias Nießner, Gordon Wetzstein, and Michael Zollhöfer. DeepVoxels: Learning Persistent 3D Feature Embeddings. *arXiv.org*, December 2018.
- [34] Xinchun Yan, Jimei Yang, Ersin Yumer, Yijie Guo, and Honglak Lee. Perspective Transformer Nets: Learning Single-View 3D Object Reconstruction without 3D Supervision. *arXiv.org*, December 2016.
- [35] Matheus Gadelha, Subhransu Maji, and Rui Wang. 3d shape induction from 2d views of multiple objects. In *2017 International Conference on 3D Vision (3DV)*, pages 402–411. IEEE, 2017.
- [36] Shubham Tulsiani, Alexei A. Efros, and Jitendra Malik. Multi-view consistency as supervisory signal for learning shape and pose prediction. In *The IEEE Conference on Computer Vision and Pattern Recognition (CVPR)*, June 2018.
- [37] Nicholas Watters, Loic Matthey, Christopher P Burgess, and Alexander Lerchner. Spatial Broadcast Decoder: A Simple Architecture for Learning Disentangled Representations in VAEs. *arXiv.org*, January 2019.
- [38] Paul Andrei Bricman and Radu Tudor Ionescu. CocoNet: A deep neural network for mapping pixel coordinates to color values. *arXiv.org*, May 2018.
- [39] William T Baxter, Robert A Grassucci, Haixiao Gao, and Joachim Frank. Determination of signal-to-noise ratios and spectral SNRs in cryo-EM low-dose imaging of molecules. *Journal of structural biology*, 166(2):126–132, May 2009.
- [40] Joseph H Davis, Yong Zi Tan, Bridget Carragher, Clinton S Potter, Dmitry Lyumkis, and James R Williamson. Modular Assembly of the Bacterial Large Ribosomal Subunit. *Cell*, 167(6):1610–1622.e15, December 2016.
- [41] Anna Yershova, Swati Jain, Steven M LaValle, and Julie C Mitchell. Generating Uniform Incremental Grids on SO(3) Using the Hopf Fibration. *The International Journal of Robotics Research*, 29(7):801–812, May 2010.
- [42] Krzysztof M Gorski, Eric Hivon, Anthony J Banday, Benjamin D Wandelt, Frode K Hansen, Mstvos Reinecke, and Matthia Bartelmann. Healpix: a framework for high-resolution discretization and fast analysis of data distributed on the sphere. *The Astrophysical Journal*, 622(2):759, 2005.

# Supplemental Information

## A Branch and bound implementation details

We perform a global search over  $SO(3) \times \mathbb{R}^2$  for the maximum-likelihood pose for each image given the current decoder MLP. Two techniques are used to improve the efficiency of the search over poses: (1) discretizing the search space on a uniform grid and sub-dividing grid points after pruning candidate poses with *branch and bound*, and (2) band pass limiting the objective to low frequency components and incrementally increasing the k-space limit at each iteration (*frequency marching*).

Our branch and bound algorithm for pose optimization is given in Algorithm 1. Briefly, we discretize  $SO(3)$  uniformly using the Hopf fibration [41] at a predefined base resolution of the grid and incrementally increase the grid resolution by sub-dividing grid points. At each resolution of the grid, the set of candidate poses is pruned using a branch and bound (BNB) optimization scheme, which alternates between a computationally inexpensive lower bound on the objective function evaluated at all grid points and an upper bound consisting of the true objective evaluated on the best lower-bound candidate. Grid points whose lower bound is higher than this value are excluded for subsequent iterations. In our case, the loss is evaluated on low-frequency components of the image; specifically, Fourier components with  $|\mathbf{k}| < k_{max}$  is an effective lower bound, as it is both inexpensive to compute and captures most of the power (and thus the error). This bound encodes the intuition that low-frequency components dominate pose estimation. We concomitantly increase  $k_{max}$  at each iteration of grid subdivision.

At each iteration, some poses are excluded by BNB, and the remaining poses are further discretized. Although BNB is risk-free in the sense that the optimal pose at a given resolution will not be pruned, our application of it is not risk-free as a candidate pose with high loss at a given resolution doesn't guarantee that its neighbor in the next iteration will not have a lower loss. Irrespective, in practice, we find that at a sufficiently fine base resolution, we obtain good results on a tractable timescale (hours on a single GPU).<sup>7</sup>

We reimplement the uniform multiresolution grids on  $SO(3)$  based on [41], using the Healpix [42] grid for the sphere and the Hopf fibration to uniformly lift the grid to  $SO(3)$ . The base grid on  $SO(3)$  contains 576 orientations. We use the ordinary grid for translations containing  $7^2$  points with an extent of 20 pixels for D=128 datasets. We subdivide the grid 5 times for a final resolution of 0.92 degrees for the orientation and 0.08 pixels for the translation. For D=64 datasets, we use a translational grid with extent of 10 pixels.

---

**Algorithm 1** CryoDRGN branch and bound with frequency marching

---

```
1: procedure OPTPHI( $\hat{X}, \hat{V}_z$ ) ▷ Find the optimal image pose given the current decoder
2:    $k_{min} \leftarrow 12, k_{max} \leftarrow D/2, N_{iter} \leftarrow 5$ 
3:    $\Phi \leftarrow SO(3) \times \mathbb{R}^2$  grid at base resolution
4:    $k \leftarrow k_{min}$ 
5:   for  $iter = 1 \dots N_{iter}$  do
6:     for  $\phi_i \in \Phi$  do ▷ Compute lower bound at all grid points
7:        $lb(\phi_i) \leftarrow$  loss between  $\hat{X}$  and SLICE( $\hat{V}_z, \phi_i$ ) at  $\mathbf{k} < k$ 
8:        $\phi^* \leftarrow \text{argmin}(lb)$ 
9:        $ub \leftarrow$  loss between  $\hat{X}$  and SLICE( $\hat{V}_z, \phi^*$ ) at  $\mathbf{k} < k_{max}$  ▷ Compute upper bound
10:       $\Phi_{new} \leftarrow \{\}$ 
11:      for  $\phi_i \in \Phi$  do ▷ Subdivide grid points below the upper bound
12:        if  $lb(\phi_i) < ub$  then
13:           $\Phi_{new} \leftarrow \Phi_{new} \cup \text{SUBDIVIDE}(\phi_i)$ 
14:       $\Phi \leftarrow \Phi_{new}$ 
15:       $k \leftarrow k + (k_{max} - k_{min}) / (N_{iter} - 1)$  ▷ Increase frequency band limit
16:  return  $\phi^*$ 
```

---

<sup>7</sup>The difference in loss between nearby poses could be incorporated into the BNB lower bound, but this would require assumptions about the smoothness of the loss with respect to pose. We leave this detail for future work.

## B Homogeneous reconstruction dataset preparation

*Simulated datasets:* We simulated datasets following the cryo-EM image formation model by 1) rotating the 3D volume in real space by  $R$ , where  $R \in SO(3)$  is sampled uniformly, 2) projecting (integrating) the volume along the z-axis, 3) shifting the resulting 2D image by  $t$ , where  $t$  is sampled uniformly from  $[-t_{min}, t_{max}]^2$  with an extent of 10 pixels for D=64 datasets, and 20 pixels for D=128 datasets, and 4) optionally adding noise to an SNR of 0.1, a typical value for cryo-EM data [39]. Following convention in the cryo-EM field, we define SNR as the ratio of the variance of the signal to the variance of the noise. We define the noise-free signal images to be the entire DxD image. The ground truth 3D volume was obtained by thresholding a volume obtained from a multiclass reconstruction of [40] and convolving the volume with a gaussian to remove sharp edges from thresholding.

*Real dataset:* To generate the real cryo-EM dataset for homogeneous reconstruction, images from EMPIAR-10028 [9] were downsampled by a factor of 4 by clipping in Fourier space. The images were then 'phase flipped' in Fourier space by their contrast transfer function, a given real-valued function with range [-1,1] determined by the microscopy conditions, i.e. the Fourier components are negated where the CTF is negative.

## C Heterogeneous ribosome

*Dataset preparation:* We consider the dataset from EMPIAR-10076 [40] which contains 131,899 images of the *E. coli* large ribosomal subunit in various stages of assembly. Images were downsampled to D=128 by clipping in Fourier space. Poses were determined by aligning the images to a mature large ribosomal subunit structure obtained from a homogeneous reconstruction of the full resolution dataset in cryoSPARC, i.e. "a consensus reconstruction".

*Baseline:* In the original analysis of this dataset [40], multiple rounds of multiclass refinement in sweeps of varying number of classes followed by expert manual alignment and clustering of similar volumes were used to identify 6 classes, labeled A-F consisting of 4 major structural states of the large ribosomal subunit (classes B-E) and 2 additional structures of the 70S and 30S ribosome, class A and F, respectively.

Since the published dataset did not contain the corresponding image cluster assignments, we perform multiclass refinement in cryoSPARC using the published structures of the 6 major states, low pass filtered to 25Å as initial models, to reproduce the results and obtain image cluster assignments. Aside from class A and F (low population impurities in the sample), the remaining structures correlate well with the published volumes (Figure S6).

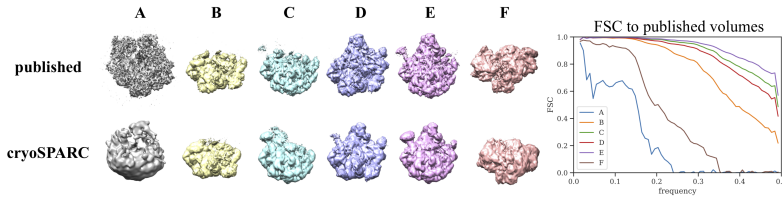


Figure S6: Reconstructed volumes from cryoSPARC multiclass refinement using the published structures of the 6 major states, low pass filtered to 25Å as initial models. Right: FSC curves between the cryoSPARC reconstructed and published volumes.

*cryoDRGN training:* We train cryoDRGN with a 1-D latent variable in minibatches of 10 images for 200 epochs, treating image pose as fixed. To simplify representation learning for  $q_\xi$ , we center and phase flip images before inputting to the encoder. We encode and decode a circle of pixels with diameter D=128 instead of the full 128x128 image.

## C.1 Validation of cryoDRGN latent encoding

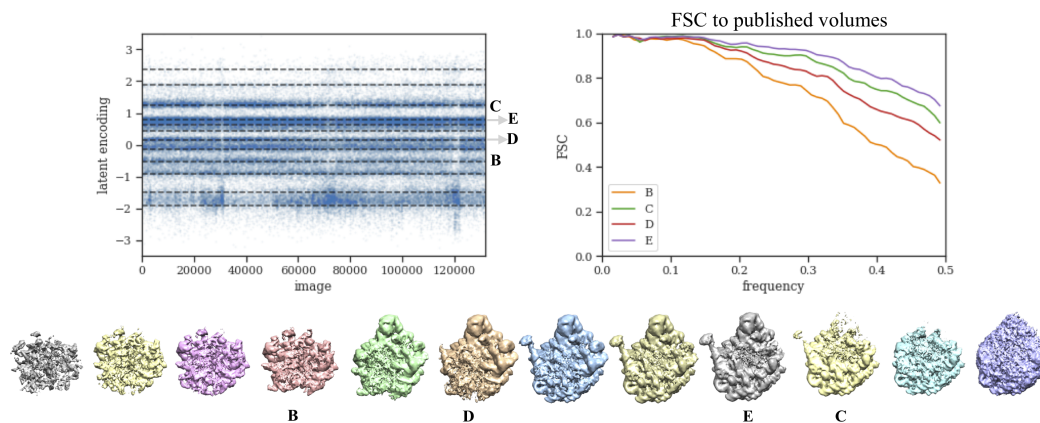


Figure S7: *Left*: Latent encoding for each image of the dataset from EMPIAR-10076. *Bottom*: Volumes from 12 sampled values along the latent space (dashed lines). *Right*: Fourier shell correlation (FSC) curves for 4 structures against the published volumes for classes B-E from [40] corresponding to structural states of the large ribosomal subunit during assembly.